Evaluation of Electrode Degradation and Projection Weld Strength in the Joining of Steel Nuts to Galvanized Advanced High Strength Steel

Pablo D. Enrique[1]
Department of Mechanical and Mechatronics Engineering,
University of Waterloo,
200 University Ave W,
Waterloo, ON, N2L 3G1, Canada
e-mail: pdenriqu@uwaterloo.ca

Hashem Al Momani
Department of Nanotechnology Engineering,
University of Waterloo,
200 University Ave W,
Waterloo, ON, N2L 3G1, Canada
e-mail: halmomani@edu.uwaterloo.ca

Christopher DiGiovanni
Department of Mechanical and Mechatronics Engineering,
University of Waterloo,
200 University Ave W,
Waterloo, ON, N2L 3G1, Canada
e-mail: ctdigiov@uwaterloo.ca

Zhen Jiao
Huys Industries Ltd,
175 Toryork Drive, Unit 35 Weston,
Toronto, ON, M9L 1X9, Canada
e-mail: fjiao@huysindustries.com

Kevin R. Chan
Huys Industries Ltd,
175 Toryork Drive, Unit 35 Weston,
Toronto, ON, M9L 1X9, Canada
e-mail: kchan@huysindustries.com

Norman Y. Zhou
Department of Mechanical and Mechatronics Engineering,
University of Waterloo,
200 University Ave W,
Waterloo, ON, N2L 3G1, Canada
e-mail: nzhou@uwaterloo.ca

Projection welding of steel weld nuts to advanced high strength steel (AHSS) in automotive applications allows for the reliable mounting of critical components with different thicknesses to the vehicle body. However, the galvanized coatings commonly used on AHSS result in electrode surface degradation during welding. In this study, the electrode degradation and its effect on the mechanical properties of welded steel nuts and AHSS sheets are investigated. Two common electrode materials are tungsten/copper and beryllium-free class III copper—both display the formation of an oxidized alloy surface layer and pitting as weld number increases. Unlike resistance spot welding, where electrodes grow in the contact area diameter as they degrade, projection welding electrodes do not experience this type of mechanical degradation. Instead, increased resistance at the electrode interface with increasing weld number results in higher temperatures at the weld interface and a larger fusion zone size, which is responsible for an observed 30% increase in weld strength over the span of 10,000 welds. [DOI: 10.1115/1.4044253]

Keywords: resistance projection welding, electrode life, galvanized coatings, advanced high strength steel, weld nuts, welding and joining

1 Introduction

Projection welding—a subset of resistance welding—is an integral part of component assembly in the automotive industry [1]. In some applications, specially designed weld nuts with projections protruding from the bottom face are welded to sheets by passing a current through the projections. High resistance at the nut and steel interfaces results in high local heat generation and either solid-state bonding or fusion zone (FZ) formation between the two parts. Similar to other resistance welding processes, the electrodes used in projection welding are consumables due to combinations of mechanical and metallurgical degradation. Although projection welding is an important and common process in industry, much of the current literature focuses on process optimization and modeling [2–5] as opposed to evaluating electrode degradation and extending electrode life. Studies of electrode degradation in similar processes, such as resistance spot welding (RSW), have attracted significantly more attention in the literature.

Electrode failure occurs for several reasons during RSW, including softening of the electrode when welding, deformation and pitting of the electrode face, and alloying of the electrode surface [6]. These are dependent on a combination of factors, including electrode geometry, electrode composition, welding parameters, and the welded material [6,7]. However, the use of a protective and corrosion-resistant Zn coating on steel is well known to further reduce electrode life [8–10]. Previous literature has shown that hard and brittle alloys can form between the Zn coating and Cu electrode, which can crack and peel with each welding cycle [11]. In some cases, increasing weld number was found to form an Al-rich layer on the electrode surface due to the progressive accumulation of Al (a secondary alloying element in Zn coatings) [8]. The formation of these alloys results in the deformation of the electrode face, which results in a decreasing current density, reduced weld nugget size, and loss in weld strength.

The effect of these Zn coatings on projection welding electrodes is unknown in the literature. Therefore, the degradation of two electrode types is studied—a tungsten/copper (W/Cu) electrode and a class III Cu electrode—by conducting 10,000 welds of three-projection steel weld nuts to galvanized (GI) coated advanced high strength steel (AHSS) sheets using each electrode. Weld strength is evaluated through torque testing, with metallographic analysis of the welds and electrode faces used to evaluate the effect of the galvanized coating on electrode degradation and weld quality. Although the electrodes experienced metallurgical and mechanical degradation, both were able to create nut-to-sheet joints that meet the minimum strength requirements over a span of 10,000 welds. With increasing weld number, the weld strength was found to increase 30%, corresponding to an increase in fusion zone size that can be explained by an increased contact resistance at the electrode surface.

2 Materials and Methods

2.1 Projection Welding Process. Welds were performed using a 250 kVA, 60 Hz single phase alternating current (AC) RSW machine fitted with projection welding electrodes. The base metal used was a 1 mm thick galvanized AHSS DP600 sheet, supplied by ArcelorMittal Dofasco. The projection nuts used were three-projection hex-flanged M6 weld nuts, as shown in Fig. 1(*a*).

[1]Corresponding author.

Manuscript received April 3, 2019; final manuscript received June 27, 2019; published online July 17, 2019. Assoc. Editor: Wayne Cai.

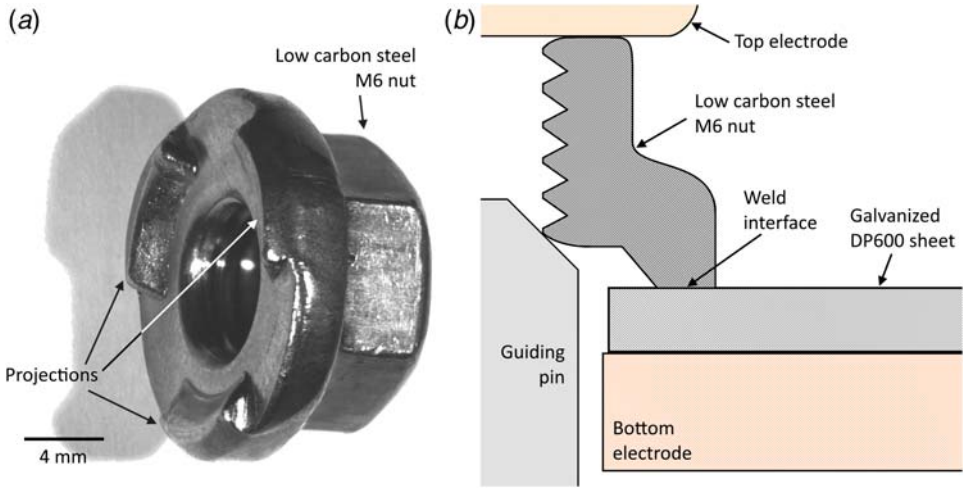

Fig. 1 (*a*) Image of projection weld nut and (*b*) schematic of projection welding setup

A schematic setup is shown in Fig. 1(*b*). The top electrode was a flat tungsten faced electrode, while the two tested bottom electrodes were made of W/Cu or class III Cu. Welds were performed on 360 mm by 126 mm DP600 sheets, prepared by punching 90 equally spaced 7.8 mm diameter holes to allow a guiding pin to pass through. Prior to each weld, a weld nut was aligned with the hole in the DP600 sheet using the guiding pin. The top electrode then applied a force on the top surface of the weld nut, and a current was passed between the electrodes. The welding parameters used (based on prior testing) were 28 kA with five cycles (one cycle = 16.67 ms), an applied force of 2 kN, and a cooling water flow rate of 4 l/min. Afterwards, a hold time of 15 cycles was used during which cooling occurs.

2.2 Electrode Design and Materials. Two different electrodes supplied by Huys Industries were used, one composed of a 75% tungsten and 25% copper mix (class 11) and the other a beryllium-free class III Cu electrode (C18000). These two materials were chosen due to their common use in resistance welding processes, with the class III Cu typically being more conductive and softer [12,13]. The physical properties of each electrode are displayed in Table 1, with hardness values obtained using a Wilson Vickers 402MVD automated hardness tester with a force of 0.98 N and a 10 s dwell time.

The bottom electrode designs also varied as shown in Fig. 2(*a*), with the W/Cu electrode having a regular industry-standard design and the class III Cu electrode having a modular design with a patent-pending swappable washer weld face. The modular design is typically used for cost saving measures in which the washer (weld face) can be replaced at end of life rather than the entire electrode (Fig. 2(*b*)).

2.3 Characterization and Testing. Microhardness measurements of cross-sectioned welds were performed using a Wilson Vickers 402MVD automated hardness tester with a 500 g load and 10 s dwell time. Etching was performed with a swabbing technique using nital, for an average etching time of 10 s. Images of the microstructure were obtained using an Oxford BX51M optical microscope (OM), and scanning electron microscopy (SEM) was performed on a Zeiss UltraPlus SEM with an energy-dispersive X-ray spectroscopy (EDX) attachment.

Table 1 Material properties of electrodes

Weld head	Weld face material	Hardness	Electrical conductivity
Regular head	W/Cu	283.5 ± 3.6 HV 0.1	42% IACS min. [14]
Modular head	Class III Cu	225.1 ± 3.0 HV 0.1	45% IACS min. [15]

Note: IACS, International Annealed Copper Standard.

Fig. 2 Bottom electrodes showing (*a*) regular head and assembled modular head and (*b*) disassembled modular head

Testing of weld strength and quality was done using torque testing. The shear load experienced during torque testing closely replicates conditions experienced in use, with failure expected when a bolt is being screwed in. A torque wrench was used to measure the maximum torque applied prior to fracture in accordance with guidelines provided by The Welding Institute, which state that the minimum torque to failure for an M6 size nut is 20 N m [16]. A minimum of 12 torque tests were performed at 200, 1000, 3000, 5000, 7000, and 10,000 welds to obtain the average torque strength.

3 Results and Discussion

3.1 Electrode Surface. Most resistance welding processes suffer from two electrode failure mechanisms: mechanical deformation of the electrode contact surface and metallurgical changes on the electrode surface [17]. Indications of both mechanisms were present on W/Cu and class III Cu projection welding electrodes, with visible signs of pitting on the surface and discoloration due to material transfer shown in Fig. 3 after 5000 welds. The formation of detrimental Cu alloys during welding [8,18] that lead to pitting is expected to be lower for the W/Cu electrode, which has significantly less Cu content. Although some pitting is still visible, the

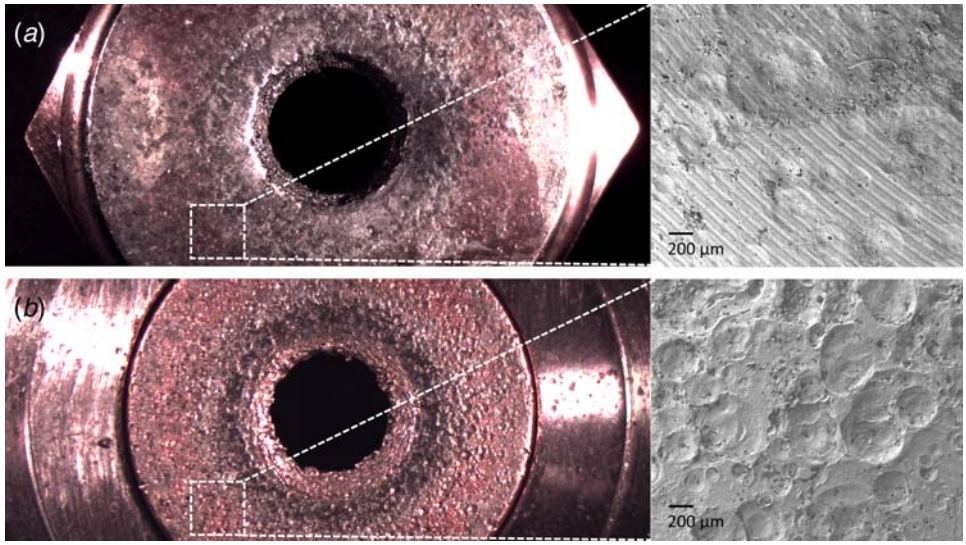

Fig. 3 Images of (*a*) W/Cu electrode surface and (*b*) class III Cu after 5000 welds, with representative SEM images and their respective locations

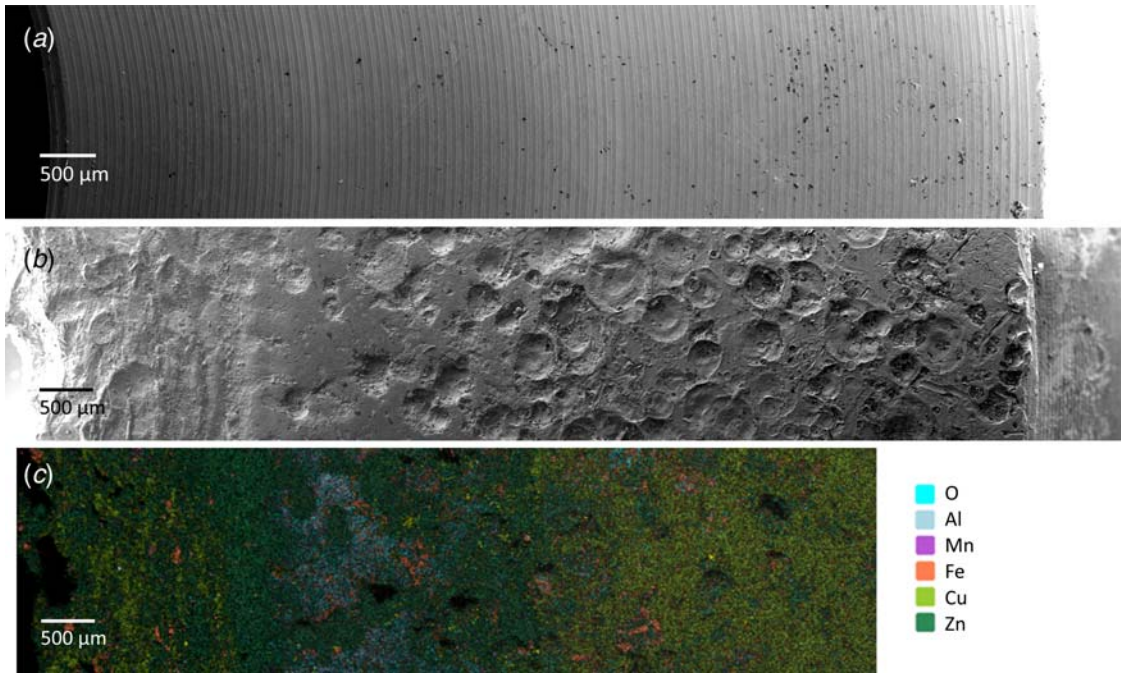

Fig. 4 SEM images of class III Cu electrode: (*a*) unused, (*b*) after 5000 welds, and (*c*) an EDX map of (*b*)

W/Cu electrode maintains some of its original machined surface (Fig. 3), which is not visible on the class III Cu electrode. Larger area SEM images of the class III Cu electrode demonstrate a significant change in roughness between the starting surface (Fig. 4(*a*)) and the used surface (Fig. 4(*b*)) at 5000 welds.

Metallurgical changes of the electrode face and the electrode face cross sections are evidenced by the EDX scans in Figs. 4(*c*) and 5, respectively. These results indicate that the discolored ring seen in Fig. 3 is primarily composed of Al, Zn, Fe, and O peaks. The source of Zn and Al can be attributed to the GI coating on the DP600 sheet, which is primarily Zn and typically contains up to 1% Al [19]. With the projection welding process occurring in an unshielded environment, this alloyed layer also appears to oxidize. The layer thickness differs significantly between the class III Cu electrode (Fig. 5(*a*)) and the W/Cu electrode (Fig. 5(*b*)) at 10,000 welds, with respective thicknesses of 6 μm and 13 μm.

An initial transfer of Zn, Fe, and Al would be expected to form brittle phases that fracture during additional welding cycles and result in pitting [18]. In RSW, this surface degradation mechanism leads to cavitation, growth of the electrode face, decrease in current density, and a decrease in nugget size that marks the end of the electrode's useful life [18,20,21]. However, in projection welding, the effective contact area onto which pressure is applied during welding is much smaller than the total electrode face. As a result, failure due to pitting, cavitation, and electrode face growth does not occur. Instead, a continuous buildup of Al, Zn, and Fe can result in an alloyed and oxidized surface with higher electrical resistivity, which has previously been identified as a challenge in the RSW of GI coated steels [22]. A quantitative analysis (Table 2) of the electrode surface alloy layers shown in Fig. 5 provides insight on the electrode degradation mechanisms and the effect of electrode composition.

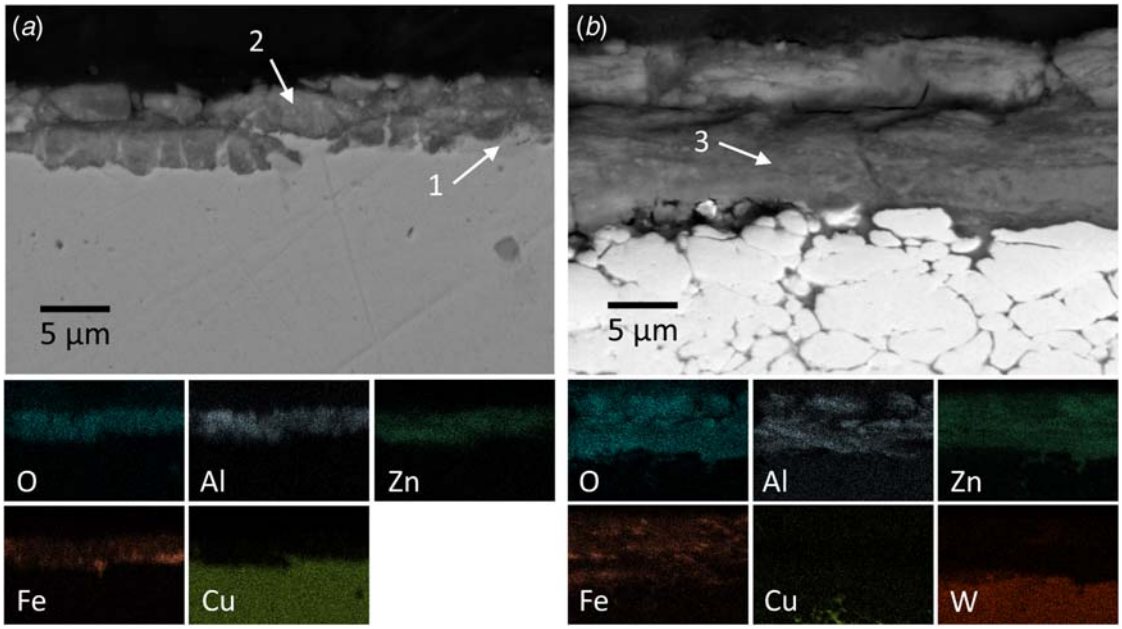

Fig. 5 SEM backscatter images of cross section along contact area in (*a*) class III Cu electrode after 10,000 welds and (*b*) W/Cu electrode after 10,000 welds

Table 2 EDX composition (at%) of alloy layers on the electrode surface as labeled in Fig. 5

	Label	O	Al	Zn	Fe	Cu	Si	Cr	Ni	W
Class III Cu	1	33.3	9.9	16.2	25.3	11.1	2.0	1.1	1.2	
	2	62.1	16.8	14.4	4.7	2.0				
W/Cu	3	53.5	9.1	29.9	5.5	0.6				1.3

After 10,000 welds, the class III Cu electrode displays two distinct layers. These are identified as labels 1 and 2 in Fig. 5 and their compositions are listed in Table 2. Both layers have consistent Zn content, with the innermost layer being Fe- and Cu-rich, and the outermost layer being Al-rich, more heavily oxidized and mostly free of Cu. The presence of Cu, Si, Cr, and Ni in the innermost layer—which are elements found within the electrode—suggests that it formed as a result of Fe and Zn alloying with the underlying Cu electrode. The formation of this typically brittle alloy layer contributes to the significant pitting visible on the class III Cu electrode. The absence of an inner layer on the W/Cu electrode is therefore attributed to the limited quantity of Cu in the electrode and lack of Fe or Zn alloying with W, which also supports the significantly lower pitting that occurs on this electrode.

The outer layer on the class III Cu electrode (label 1) and only layer on the W/Cu electrode (label 3) are similar in their high oxygen and low Fe and Cu content. The formation of this layer on both electrodes suggests that it is not dependent on the underlying electrode composition. Variation in outer alloy layer composition between the two electrodes is attributed to regional variability, with Fig. 4(*c*) showing that some regions are Al-rich while others are Zn-rich. This variation is likely the result of Zn being squeezed outwards from the contact areas that experience the highest pressure and greatest heating during welding. When zinc is pushed outwards, it can expose a thin aluminide found between the Zn coating and DP600 sheet [23], allowing Al to more easily transfer and concentrate on the electrode. The effect of an oxidized Al-rich and Zn-rich electrode surface on projection weld quality requires an evaluation of the weld microstructure and a measure of the weld strength as a function of weld number.

3.2 Weld Strength and Microstructure. To evaluate the primary failure mode of projection welded nuts (failure due to shear as a screw is tightened), torque tests are performed at various weld number intervals. Both electrode materials formed welds with similar strengths, suggesting that no reduction in weld quality occurred as a result of the differences in conductivity, weld face hardness, alloy layer thickness, and extent of pitting. However, torque strength was found to increase with increasing weld number (Fig. 6), specifically between 1000 and 5000 welds.

During projection welding, the projections on the bottom of the steel nut collapse due to a combination of pressure and current applied by the welding electrodes. The resulting localized heating, melting, and solidification forms the FZ that joins the two materials. An example of a weld cross section made with a class III Cu electrode (weld number 5000) is provided in Fig. 7(*a*), with no significant variation in microstructure observed between welds made with W/Cu and class III Cu electrodes.

For welds created using both electrode types, no noticeable differences in hardness were observed (example provided in Fig. 7(*b*)). FZ hardness was equivalent to the heat affected zone (HAZ) hardness in DP600 (average and standard error of 428 ± 6 μm and 421 ± 7 μm, respectively) but could be visually discerned by the columnar microstructure that forms during solidification in the FZ. The equivalent hardness is attributed to the lath martensite (Fig. 8) that forms during welding. However, the DP600 base metal (BM) and nut BM are significantly softer due to the lack of martensite, with both the DP600 BM and nut BM having similar hardness (214 ± 5 μm versus 215 ± 4 μm, respectively). The higher hardness and lower ductility in the FZ and DP600 HAZ are expected to be the fracture location for projection welded nuts and can be evaluated by analyzing the fracture surfaces of nuts torqued to failure.

When viewing the DP600 sheet fracture surface for welds made at lower weld number (1000), combinations of smooth and rough regions along the projection contact area are present. Smooth features (Fig. 9(*a*), region 2) indicate regions that are unbonded, likely the result of insufficient heat generation at the interface during welding. However, the circular features (Fig. 9, regions 1 and 3) show small, shallow dimple-like features that suggest a fracture with limited ductility and can be attributed to fusion zone formation between the nut and the sheet. Also visible is an increase in the size of the fusion zone between Figs. 9(*a*) and 9(*b*). This indicates the formation of larger weld nuggets with increasing weld

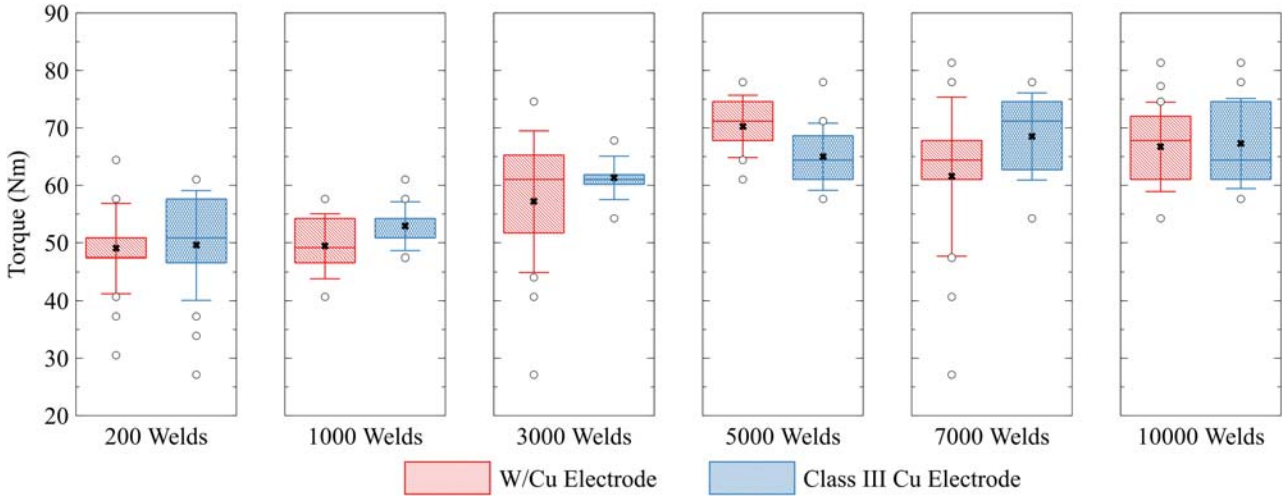

Fig. 6 Torque testing results for M6 nuts projection welded to DP600 steel using W/Cu and Class III Cu electrodes, with boxes indicating second and third quartiles, mean values indicated with an "x," and whiskers indicating 1 standard deviation from the mean

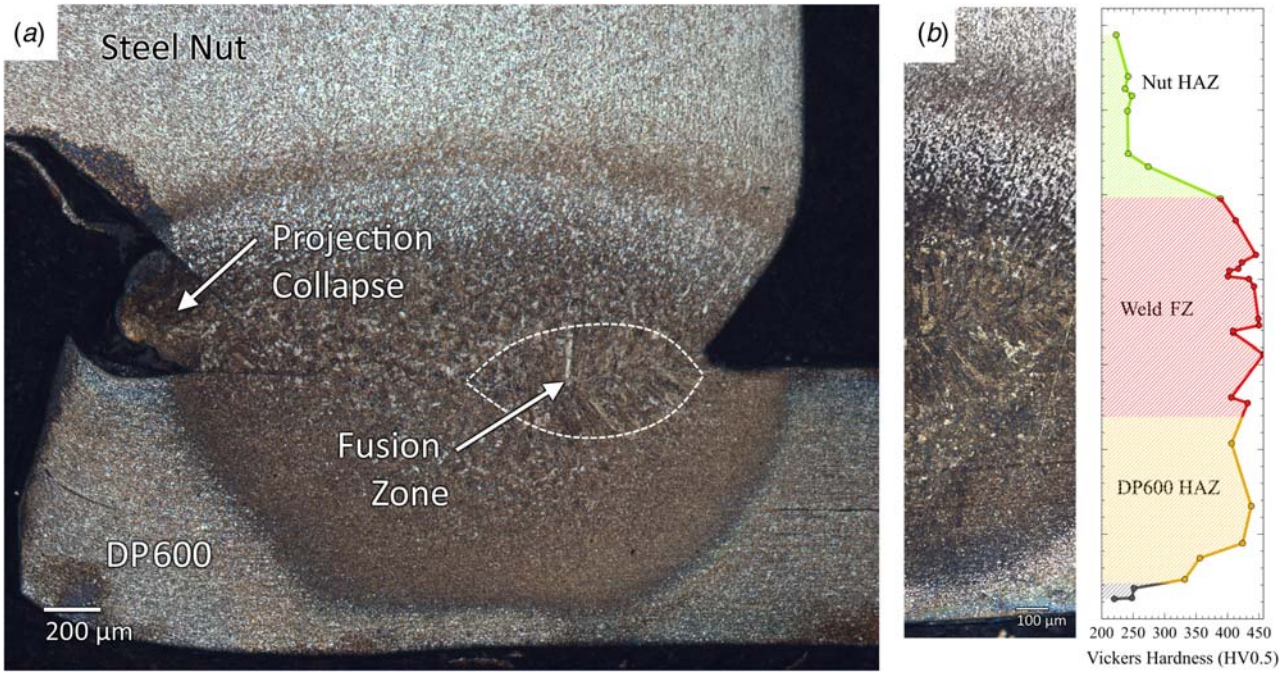

Fig. 7 Example of a projection weld between a steel nut and a DP600 sheet made with a class III Cu electrode: (*a*) showing material extrusion due to projection collapse and weld nugget formation in the FZ and (*b*) the hardness profile along the cross section

number, which explains the increased weld strength between 1000 and 5000 welds seen in Fig. 6. Larger weld nuggets can distribute the stress of an applied force over a greater area, so that failure occurs at a higher applied torque.

Larger fusion zone formation can be attributed to greater heat generation during welding. This can be seen in the larger size and shape of the HAZs, and greater material extrusion at higher weld numbers. Figure 10(*b*) shows what appears to be two overlapping HAZs, one originating from the nut/DP600 interface and the other originating from the DP600/electrode interface. With alloying and oxidation on the electrode surface, increased heat generation during welding and reduced thermal conduction through the electrode are expected due to greater contact resistance. Similar results have been reported for TiC-coated RSW electrodes, which lead to larger weld sizes than uncoated electrodes when using identical weld parameters [24], or in the case of welds performed with thin metal strips between the workpiece and electrode [25].

The high electrical resistivity and low thermal diffusion of the alloyed and oxidized electrode surface—as well as pitting on the electrode surface—are expected to increase the contact resistance and decrease the thermal diffusion at the sheet/electrode interface. To investigate the effect of this increased contact resistance on the temperature at the weld interface, a simplified 1D simulation of heat conduction and internal heating during welding is performed. Under the assumption that there is no heat transfer in the y or z direction, the progression in time (t) between the temperature (T) along the weld profile (x) is expressed as

$$\frac{\partial T}{\partial t} = \alpha\left(\frac{\partial^2 T}{\partial x^2} + \frac{\dot{g}}{k}\right) \tag{1}$$

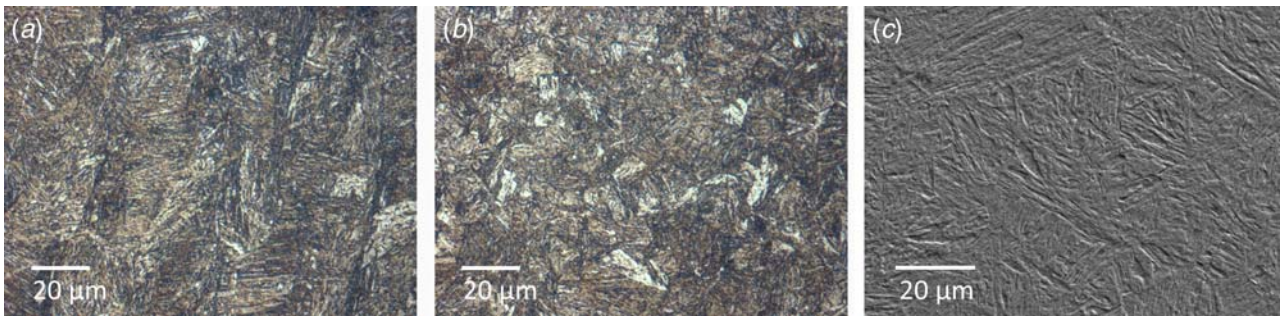

Fig. 8 Images of (*a*) microstructure in columnar FZ, (*b*) microstructure in equiaxed DP600 HAZ, and (c) SEM image of the lath martensite present in both (*a*) and (*b*)

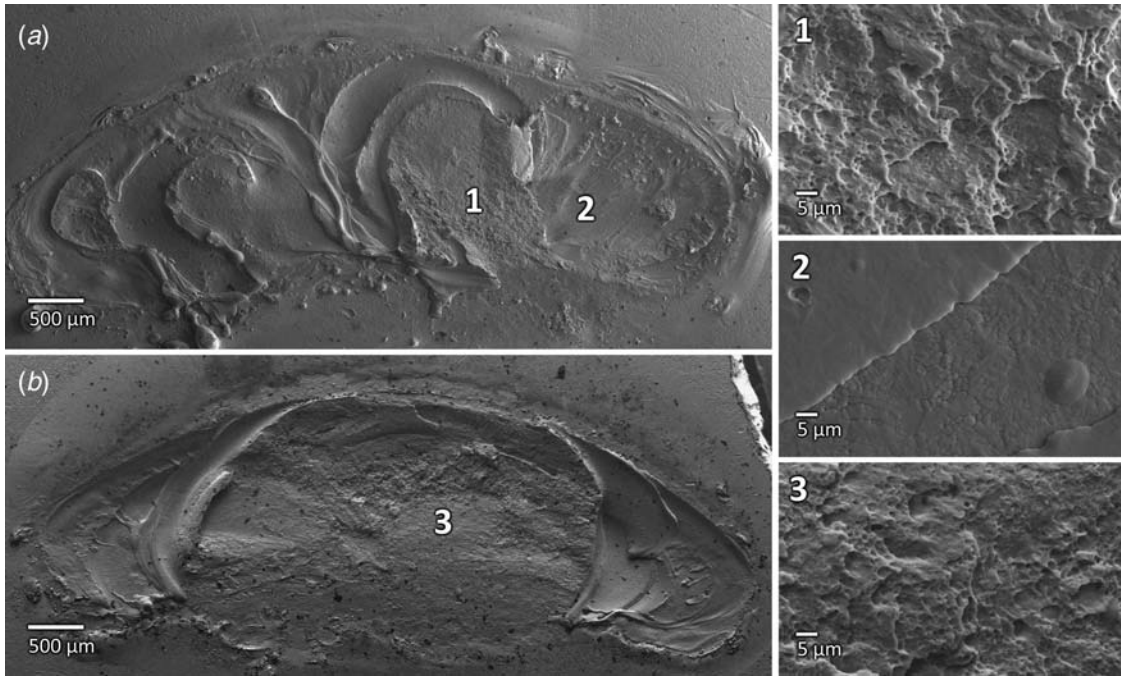

Fig. 9 SEM images of fractured DP600 sheets welded with class III Cu electrodes after torque testing with weld numbers of (*a*) 1000 and (*b*) 7000

where α is the thermal diffusivity, $\dot{g}$ is the volumetric rate of heat generation, and k is the thermal conductivity [26]. To simulate the use of cooling water along the top and bottom electrodes, a Dirichlet boundary condition is implemented on the top and bottom boundaries ($T = 283.15\ K$). This assumes that the water flow rate is enough to maintain the electrode/water boundaries at the same temperature as the water. All other nodes are set to an initial room temperature condition ($T = 298.15\ K$). During the first five cycles in which welding occurs, the joule heating of the electrodes, nut, DP600 sheet, the nut/sheet weld interface, and the sheet/electrode interface is considered as follows:

$$\dot{g} = \left(\frac{I}{3}\right)^2 \frac{R}{V} \tag{2}$$

where I is the input current, V is the volume of the material, and R is the resistance. Since the three projections on each weld nut are considered parallel resistors, one-third of the input current flows through each nut/sheet weld interface. The bulk and contact resistance are calculated according to Eqs. (3) and (4), respectively, which are based on the expressions for joule heating and constriction resistance [27,28]

$$R = \frac{\rho \Delta x}{A} \tag{3}$$

$$R = 0.89\rho\left(\frac{\xi H}{\eta F}\right)^{1/2} \tag{4}$$

where ρ is the electrical resistivity, A is the cross-sectional area, H is the material hardness, F is the applied force by the electrodes during welding, ξ is a pressure factor with a typical value of 0.7, and η is the contact spots factor, which has a value of 1 for a polished, ideal surface. As the weld number increases and the electrode undergoes pitting, the value of η is expected to decrease. Similarly, as alloying and oxidation occurs on the electrode surface, ρ and H are expected to increase. These changes have the effect of increasing the contact resistance.

After the initial five cycles of welding, the internal heat generation term $\dot{g}$ is set to zero and the material is allowed to cool for 15 cycles. To solve Eq. (1), the geometry of a projection weld nut and sheet is simplified as shown in Fig. 11(*a*) and no consideration is given to the GI coating along the top and bottom boundaries of the steel sheet. Additionally, Eq. (4) is only used to include the interface resistance at the nut/sheet and sheet/electrode interface,

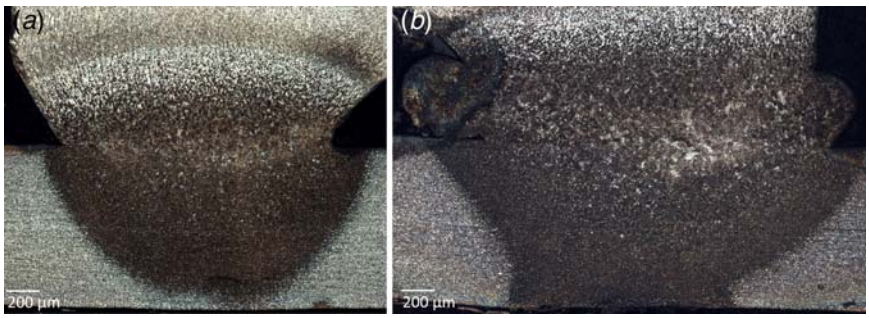

Fig. 10 OM images of etched, cross-sectioned welds corresponding to weld number (*a*) 1000 and (*b*) 5000

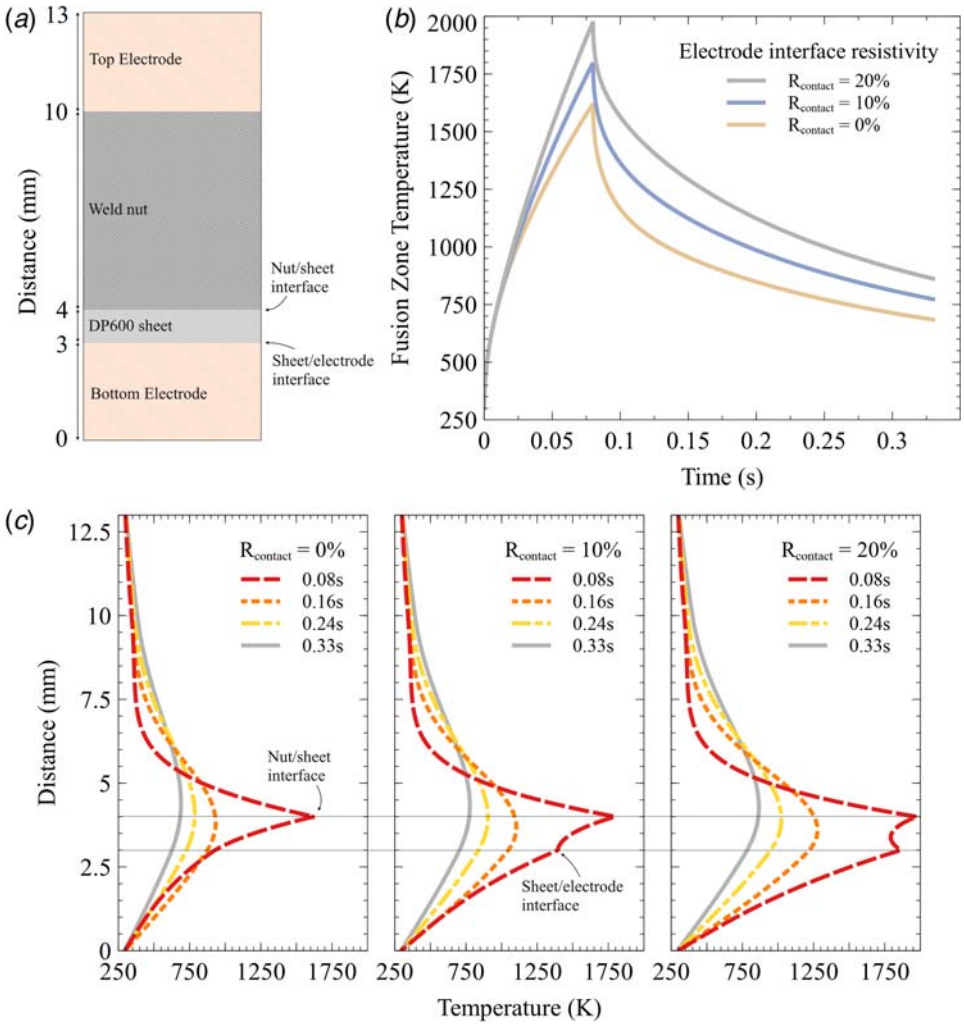

Fig. 11 (*a*) Simplified geometry of the projection welding profile, (*b*) simulation results for fusion zone temperature with varying contact resistance at the sheet/electrode interface relative to contact resistance at the nut/sheet interface, and (c) temperature along the weld profile after welding and during cooling for varying contact resistance

which assumes that no heat is generated at the top electrode's surface. This approximation is considered appropriate due to the lack of observed metallurgical and mechanical degradation at the top electrode, attributed to the significant distance from the fusion zone. With these approximations, Eq. (1) is solved in MATLAB through a method of lines approach, in which the spatial dimension is discretized, and time dimension is solved using a built-in differential equation solver (ode45).

The influence of an increasing contact resistance on the fusion zone temperature is shown in Fig. 11(*b*), where the contact resistance used in Eq. (4) to model heat generation at the sheet/electrode interface is increased up to 20% of the contact resistance at the nut/sheet interface. A relative contact resistance of 0% reflects an unused electrode with no oxide or pitting on the surface, such that no additional internal heat is generated at the sheet/electrode interface. As seen in the case of a relative resistance of 10% and

20%, increased resistance at the sheet/electrode interface can significantly increase the nut/sheet interface temperature, which increases the amount of melted material and results in larger fusion zone formation (Fig. 11(*c*)).

Although electrode failure was not observed within this study, further increases in the contact resistance due to increased alloying and oxide formation are expected to further increase the temperature within the fusion zone. This may result in excessive expulsion of molten material that creates voids within the fusion zone, which lowers the weld strength. This failure mode in projection welding can be mitigated by lowering the current with increasing weld number (opposite to how electrode wear is compensated for in RSW [29]), which can also be used to maintain a consistent weld strength throughout the electrode life. However, although some expulsion does occasionally occur during welding, no failures were identified up to the tested 10,000 welds and no definitive electrode life was established.

4 Conclusions

The degradation of two projection welding electrode types—a regular W/Cu electrode and modular class III Cu electrode—was evaluated by performing 10,000 welds of steel weld nuts to galvanized advanced high strength steel (DP600). Both electrodes produced projection welds with similar strengths, and an increasing strength with increasing weld number was observed.

- Torque testing results show an increase in weld strength of approximately 30% between 1000 and 5000 welds using either electrode. No decline in strength was measured between 5000 and 10,000 welds, and no difference in strength is measured between the welds created with the W/Cu electrode and the class III Cu electrode, with all welds passing the minimum acceptable torque strength.
- Two primary electrode degradation mechanisms are observed. Fe, Zn, and Al are transferred from the galvanized DP600 sheet and build up on the electrode surface, resulting in metallurgical degradation. Due to the high temperatures obtained during welding, the alloy layer oxidizes and forms a 13 μm thick coating on the W/Cu electrode and a 6 μm coating on the class III Cu electrode after 10,000 welds. Mechanical degradation also occurs, with greater pitting on the class III Cu electrode.
- Increased heat generation and decreased heat transfer due to oxide formation and pitting are expected to result in higher temperatures during welding, larger fusion zones, and larger heat-affected zones. Greater fusion zone size explains the increase in weld strength with increasing weld number as an alloy forms and oxidizes on the electrode surface and as the extent of pitting increases. Modeling of thermal conduction and internal heat generation during welding suggests that heat generation at the sheet/electrode interface can explain the formation of larger fusion zones due to the corresponding increase in fusion zone temperatures.

Acknowledgment

This work was performed at the Centre for Advanced Materials Joining (CAMJ) at the University of Waterloo with funding support from the Natural Sciences and Engineering Research Council of Canada (NSERC) (Funder ID: 10.13039/501100000038), the Canada Research Chairs (CRC) Program (Funder ID: 10.13039/501100001804), Huys Industries, and the CWB Welding Foundation.

References

[1] Larsson, J., 2008, Projection Welding for Nut and Bolt Attachment: Competing or Complementary Joining Methods?. The Fabricator. https://www.thefabricator.com/article/shopmanagement/projection-welding-for-nut-and-bolt-attachment, Accessed November 2, 2018.
[2] Nielsen, C. V., Zhang, W., Martins, P. A. F., and Bay, N., 2015, "3D Numerical Simulation of Projection Welding of Square Nuts to Sheets," J. Mater. Process. Technol., **215**(1), pp. 171–180.
[3] Mikno, Z., 2018, "Projection Welding of Nuts Involving the Use of Electromechanical and Pneumatic Electrode Force," Int. J. Adv. Manuf. Technol., **99**(5–8), pp. 1405–1425.
[4] Ha, S., Murugan, S. P., Marimuthu, K. P., Park, Y., and Lee, H., 2019, "Estimation of Lobe Curve With Material Strength in Resistance Projection Welding," J. Mater. Process. Technol., **263**(Aug.), pp. 101–111.
[5] Tolf, E., and Hedegård, J., 2007, "Resistance Nut Welding: Improving the Weldability and Joint Properties of Ultra High Strength Steels," Weld. World, **51**(3–4), pp. 28–36.
[6] Davies, G., 2012, *Materials for Automobile Bodies*, Elsevier, New York.
[7] Bowers, R., Sorensen, C., and Eagar, T., 1990, "Electrode Geometry in Resistance Spot Welding," Weld. J., **69**(2), pp. 45–51.
[8] Parker, J. D., Williams, N. T., and Holliday, R. J., 1998, "Mechanisms of Electrode Degradation When Spot Welding Coated Steels," Sci. Technol. Weld. Join., **3**(2), pp. 65–74.
[9] Chen, Z., Zhou, Y., and Scotchmer, N., 2006, "Coatings on Resistance Welding Electrodes to Extend Life," SAE 2006 World Congress & Exhibition, Detroit, MI.
[10] Zou, J., Zhao, Q., and Chen, Z., 2009, "Surface Modified Long-Life Electrode for Resistance Spot Welding of Zn-Coated Steel," J. Mater. Process. Technol., **209**(8), pp. 4141–4146.
[11] Kondo, M., Konishi, T., Nomura, K., and Kokawa, H., 2013, "Degradation Mechanism of Electrode Tip During Alternate Resistance Spot Welding of Zinc-Coated Galvannealed and Uncoated Steel Sheets," Weld. Int., **27**(10), pp. 770–778.
[12] Davis, J. R., 2001, *ASM Specialty Handbook: Copper and Copper Alloys*, ASM International, Materials Park, OH.
[13] Deffenbaugh, J. F., 2003, *Resistance Welding Manual*, Resistance Welder Manufacturers' Association, Philadelphia, PA.
[14] Sherbrooke Metals, "Elkonite Copper Tungsten," http://www.sherbrookemetals.com/elkonite-r-copper-tungsten-2
[15] Cadi Company Inc., "Copper Nickel Silicon Chromium C18000 Class 3," http://www.cadicompany.com/products-C18000-copper-nickel-silicon-chromium.php
[16] The Welding Institute, "FAQ: What are the Guidelines for Projection Welding Weld-Nuts?" https://www.twi-global.com/technical-knowledge/faqs/faq-what-are-the-guidelines-for-projection-welding-weld-nuts, Accessed February 13, 2019.
[17] Babu, S., Santella, M., and Peterson, W., 2004, "Modeling Resistance Spot Welding Electrode Life," AWS Welding Shows, Chicago, IL.
[18] Lum, I., Biro, E., Zhou, Y., Fukumoto, S., and Boomer, D. R., 2004, "Electrode Pitting in Resistance Spot Welding of Aluminum Alloy 5182," Metall. Mater. Trans. A, **35**(1), pp. 217–226.
[19] Marder, A. R., 2000, "The Metallurgy of Zinc-Coated Steel," Prog. Mater. Sci., **45**(3), pp. 191–271.
[20] Tumuluru, M., 2010, "Resistance Spot Weld Performance and Weld Failure Modes for Dual Phase and TRIP Steels," *Failure Mechanisms of Advanced Welding Processes*, X. Sun, ed., Woodhead Publishing Limited, Cambridge, UK, pp. 43–64.
[21] Chang, B. H., Zhou, Y., Lum, I., and Du, D., 2005, "Finite Element Analysis of Effect of Electrode Pitting in Resistance Spot Welding of Aluminium Alloy," Sci. Technol. Weld. Join., **10**(1), pp. 61–66.
[22] Tumuluru, M., 2007, "The Effect of Coatings on the Resistance Spot Welding Behavior of 780 MPa Dual-Phase Steel," Weld. J., **86**(June), pp. 161–169.
[23] Furdanowicz, V., and Shastry, C. R., 1999, "Distribution of Aluminum in Hot-Dip Galvanized Coatings," Metall. Mater. Trans. A Phys. Metall. Mater. Sci., **30**(12), pp. 3031–3044.
[24] Chan, K. R., Scotchmer, N., Zhao, J., and Zhou, Y., 2010, "Weldability Improvement Using Coated Electrodes for RSW of HDG Steel," SAE Technical Paper Series, **1**(724).
[25] Zhao, Y., Zhang, Y., Lai, X., and Wang, P.-C., 2013, "Resistance Spot Welding of Ultra-Thin Automotive Steel," ASME J. Manuf. Sci. Eng., **135**(2), p. 021012.
[26] Montecucco, A., Buckle, J. R., and Knox, A. R., 2012, "Solution to the 1-D Unsteady Heat Conduction Equation With Internal Joule Heat Generation for Thermoelectric Devices," Appl. Therm. Eng., **35**(1), pp. 177–184.
[27] Hamedi, M., and Atashparva, M., 2017, "A Review of Electrical Contact Resistance Modeling in Resistance Spot Welding," Weld. World, **61**(2), pp. 269–290.
[28] Holm, R., 1967, *Electric Contacts*, Springer, Berlin.
[29] Li, W., 2004, "Modeling and On-Line Estimation of Electrode Wear in Resistance Spot Welding," ASME J. Manuf. Sci. Eng., **127**(4), pp. 709–717.